Hierarchical VO2@BiVO4 Films Decorated With Porous BiVO4 Nanoplates for Durable and Self-Cleaning Smart Windows

Rare Metals

WILEY | 有科出版 YOUKE PUBLISHING

ORIGINAL ARTICLE OPEN ACCESS

Hierarchical VO_2@$BiVO_4$ Films Decorated With Porous $BiVO_4$ Nanoplates for Durable and Self-Cleaning Smart Windows

Huiyan Xu[1] | Lihan Cai[2] | Jian Zhang[3] | Rui Chen[1] | Zaoyang Xu[1] | Mingyu Lu[1] | Xinyuan Xing[1] | Shuaijun Yang[1] | Tongyao Liu[1] | Yuanwei Sun[4,5] | Xuchuan Jiang[1] | Xin Yu[2]

[1]Institute for Smart Materials & Engineering, University of Jinan, Jinan, China | [2]Institute for Advanced Interdisciplinary Research (iAIR), School of Chemistry and Chemical Engineering, University of Jinan, Jinan, China | [3]Division of Systems and Synthetic Biology, Department of Life Sciences, Chalmers University of Technology, Goteborg, Sweden | [4]Medical Science and Technology Innovation Center, Jinan, China | [5]Electron Microscopy Center, Shandong First Medical University and Shandong Academy of Medical Sciences, Jinan, China

Correspondence: Xin Yu (ifc_yux@ujn.edu.cn) | Xuchuan Jiang (ism_jiangxc@ujn.edu.cn) | Yuanwei Sun (ywsun@sdfmu.edu.cn)

Received: 26 November 2025 | **Revised:** 26 January 2026 | **Accepted:** 28 January 2026

Keywords: $BiVO_4$/VO_2@$BiVO_4$ | hierarchical structure | self-cleaning | smart window | thermochromism

ABSTRACT

VO_2 is a promising thermochromic material, but it is still limited by low transparency, weak solar modulation, and poor stability. Here, we develop a coordination-compound-derived strategy to construct a hierarchical $BiVO_4$/VO_2@$BiVO_4$ film with a core–shell@nanosheet structure. VO_2@$BiVO_4$ nanoparticles form the inner layer, whereas porous $BiVO_4$ nanosheets assemble on the surface. This architecture provides synergistic benefits: The $BiVO_4$ shell protects VO_2 from oxidation and enhances plasmon-induced solar modulation, and the nanosheets improve visible transparency via antireflection. The composite also exhibits photocatalytic self-cleaning and antibacterial activity. It delivers 63.0% visible transmittance and 15.6% solar modulation, retaining 80% performance after 27 days at 100°C and 50% humidity. This work integrates optical performance, durability, and multifunctionality, offering a practical pathway for VO_2-based smart windows.

1 | Introduction

Smart window materials, which can modulate light transmittance in response to ambient temperature, hold significant potential for energy-efficient building applications [1–3]. Vanadium dioxide (VO_2) is a prototypical thermochromic material that undergoes a reversible metal-insulator transition around 68°C [4–6]. Below the critical temperature, VO_2 adopts a phase, causing a sharp decrease in near-infrared transmittance with minimal change in visible-light transmission [7–9]. This unique feature enables VO_2 to modulate solar heat gain while maintaining indoor brightness, making it an attractive candidate for smart window applications. However, conventional VO_2 films face critical challenges: Achieving both high visible-light luminous transmittance (T_{lum}) and strong solar modulation ability (ΔT_{sol}) is difficult, and VO_2 is prone to oxidation and aggregation, which compromise environmental stability [10–12]. Its intrinsic coloration further limits light transmission, restricting practical deployment [13–15].

Compositing VO_2 with functional materials has emerged as an effective strategy to overcome these limitations [16–18]. Multilayer structures, such as Cr_2O_3/VO_2/SiO_2 films, improve T_{lum} and ΔT_{sol} through antireflection effects while enhancing durability, yet their complex fabrication and high cost hinder scalability [19–21]. Inorganic nanoparticle blending offers a simpler, cost-effective alternative, improving VO_2 dispersion and exploiting localized surface plasmon resonance to enhance ΔT_{sol}. For instance, ZnO/VO_2 composites show significant increases in T_{lum} and ΔT_{sol}, whereas sol-gel SiO_2 blends yield

similar improvements [22–29]. Nonetheless, current hybrid coatings still lack micro/nanostructural diversity, limiting further performance optimization.

Vanadates, such as $BiVO_4$, provide versatile micro/nanostructures, including nanosheets, nanorods, and hierarchical architectures that reduce surface reflectance and enhance visible-light transmittance [30–34]. $BiVO_4$ also exhibits strong photocatalytic activity, enabling self-cleaning and antibacterial functions [35–37], which can improve VO_2 stability and reduce maintenance requirements.

Here, we report a hierarchically structured composite coating comprising porous $BiVO_4$ nanosheets and VO_2@$BiVO_4$ core–shell nanoparticles. The outer $BiVO_4$ nanosheets reduce surface reflection, enhancing visible-light transmittance, whereas the $BiVO_4$ shells stabilize VO_2 dispersion and improve optical uniformity. The photocatalytic activity of $BiVO_4$ further imparts self-cleaning and antibacterial capabilities, decomposing organic contaminants and inhibiting bacterial adhesion, thereby enhancing coating durability. As a result, the composite achieves an excellent balance of optical performance (T_{lum} = 63.0%, ΔT_{sol} = 15.6%) and stability, retaining ~80% of modulation capacity after 27 days at 100°C and 50% relative humidity. This work demonstrates a structure-function integrated design that advances VO_2-based smart windows toward multifunctional, high-transmittance, and durable energy-saving applications.

2 | Experimental

2.1 | Preparation of Precursor Solution

4.6 g of vanadium pentoxide (V_2O_5) and 4.6 g of oxalic acid dihydrate were dissolved in 100 mL of anhydrous ethanol and refluxed in an oil bath at 100°C for 12 h. The solution color gradually changed from yellowish brown to bluish green. Afterward, it was left to stand at room temperature for 24 h. The supernatant was then collected, and different amounts of bismuth sulfate were added to achieve Bi/(Bi + V) molar ratios of 0%, 10%, 20%, and 30%.

2.2 | Preparation of $BiVO_4$/VO_2@$BiVO_4$ Composite Coatings

The obtained precursor solution was spin-coated onto glass substrates, naturally dried, and then annealed at 400°C for 2 h to obtain $BiVO_4$/VO_2@$BiVO_4$ composite coatings.

3 | Results and Discussion

3.1 | Morphology and Structure of the Coatings

First, Figure 1A schematically illustrates the preparation of the $BiVO_4$/VO_2@$BiVO_4$ composite coatings via a sol-gel method. In the absence of $Bi_2(SO_4)_3$ in the precursor, the resulting coating consists of densely packed nanoparticles (Supporting Information S1: Figure S1). Upon addition of $Bi_2(SO_4)_3$, the coating surface transforms into a porous nanosheet morphology (Figure 1B). Cross-sectional SEM images reveal a bilayer structure, comprising a top layer of porous nanosheets and a bottom layer of nanoparticles (Figure 1C). EDS analysis of Region I in Figure 1D indicates a higher atomic ratio of V (8.5%) than Bi (5.4%), confirming that the bottom layer is primarily composed of VO_2. In contrast, EDS analysis of Region II (Figure 1E) shows a V:Bi molar ratio of approximately 1:1, consistent with the stoichiometry of $BiVO_4$, verifying that the nanosheet layer consists of $BiVO_4$.

TEM images (Figure 1F) reveal clear contrast between $BiVO_4$/VO_2@$BiVO_4$ composite particles and the surrounding matrix, indicating a core–shell structure. The sizes of the core and shell are 72 and 9 nm, respectively. High-resolution TEM (HRTEM) of the core region (Figure 1G and Region I in Figure 1F) shows lattice fringes with a spacing of ~3.25 Å, corresponding to the (011) plane of VO_2, whereas the shell appears amorphous or disordered. The selected-area fast Fourier transform (FFT) and the corresponding simulated electron diffraction (ED) patterns for the core region are presented in Supporting Information S1: Figure S3. The FFT pattern aligns closely with the simulated ED pattern of VO_2, indicating a high degree of consistency, reinforcing the existence of VO_2. HRTEM of the nanosheet layer (Figure 1H, Region II in Figure 1F) exhibits lattice fringes with a spacing of ~3.11 Å, corresponding to the (112) plane of $BiVO_4$, confirming its crystalline structure. Elemental mapping (Figure 1I) further demonstrates that the shell is enriched in Bi, whereas the core is rich in V and O, corroborating the core–shell architecture.

X-ray diffraction (XRD) patterns show that, without $Bi_2(SO_4)_3$, only the monoclinic VO_2 (011) peak (JCPDS No. 43-1051) is detected (Figure 1J). After incorporating $Bi_2(SO_4)_3$, additional diffraction peaks corresponding to the (101), (112), and (004) planes of $BiVO_4$ (JCPDS No. 48-0744) emerge, in agreement with TEM and EDS results. Wide-scan X-ray photoelectron spectroscopy (XPS) confirms the presence of V, Bi, and O elements in the coating (Supporting Information S1: Figure S2). High-resolution V 2p spectra display a peak at 517.0 eV, corresponding to V^{5+} in the $BiVO_4$ shell, consistent with VO_2 being encapsulated (Figure 1K) and the ~10 nm probing depth of XPS. Bi 4f spectra show peaks at 159.4 and 164.7 eV, attributed to Bi^{3+} in $BiVO_4$ (Figure 1L). The O 1s spectrum reveals contributions from lattice oxygen (O_L), chemisorbed oxygen (O_C), and oxygen vacancies (O_V), indicating a complex oxygen environment within the composite coating (Figure 1M).

To elucidate the formation mechanism of the hierarchical micro-nano structure in the composite coatings, the morphological evolution of the films under different annealing durations was investigated. After 30 min of thermal treatment, the coating exhibited a porous structure, but nanosheets had not yet formed (Figure 2A). At 60 min, the pore size increased, and a coexistence of nanosheets and nanoparticles appeared (Figure 2B). After 90 min, the number of nanosheets decreased, and they gradually merged with the nanoparticles (Figure 2C). At 120 min, the nanoparticles and nanosheets fully fused into a uniform structure (Figure 2D). Figure 2E–H shows the corresponding changes in film thickness with annealing time. The

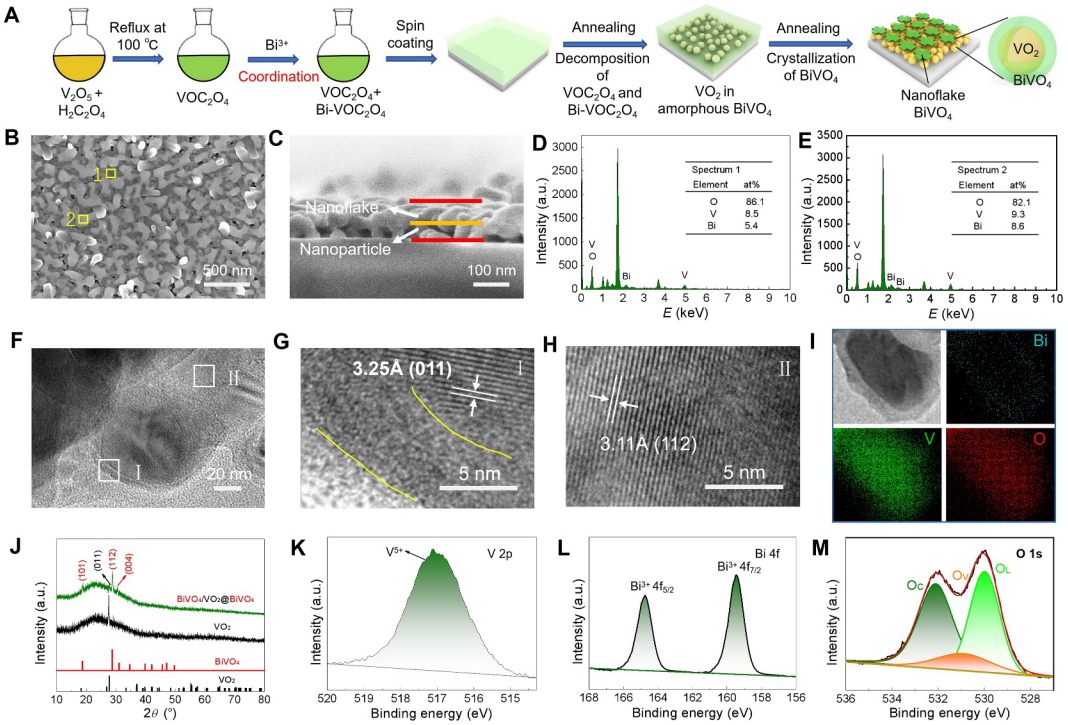

FIGURE 1 | Structural design, morphology, and composition characterization of the hierarchical $BiVO_4/VO_2$@$BiVO_4$ composite coating. (A) Schematic illustration of the preparation of $BiVO_4/VO_2$@$BiVO_4$ composite coatings. (B) SEM image of $BiVO_4/VO_2$@$BiVO_4$ and (C) its cross-sectional view. EDS spectra of (D) the nanosheet layer and (E) the nanoparticle layer in the composite coating. (F) TEM image of the composite coating; HRTEM images of (G) the nanoparticle core and (H) the nanosheet layer; (I) elemental mapping of the nanoparticles. (J) XRD patterns of VO_2 and $BiVO_4/VO_2$@$BiVO_4$. XPS spectra of the $BiVO_4/VO_2$@$BiVO_4$ composite coating: (K) V 2p, (L) Bi 4f, and (M) O 1s.

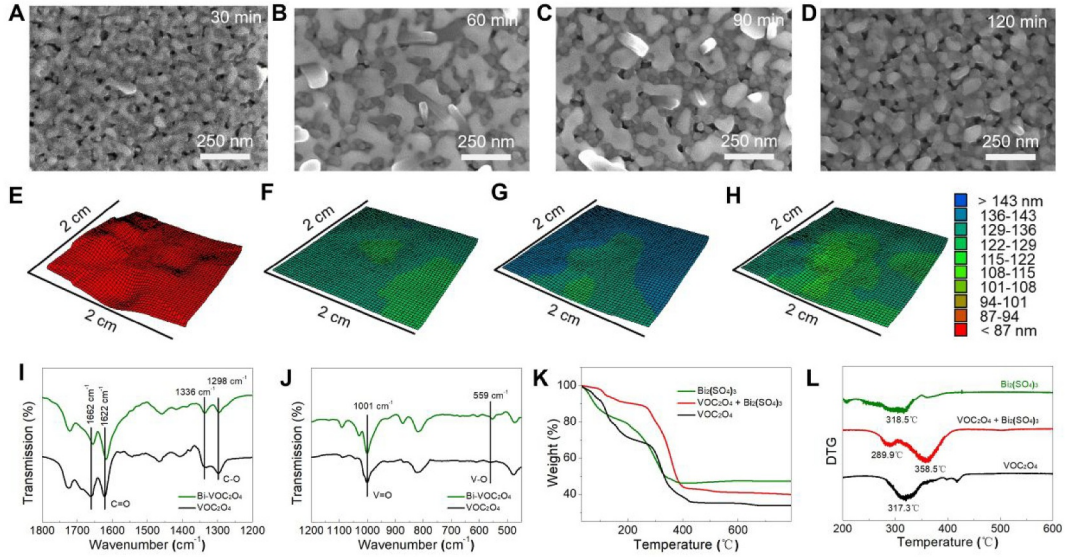

FIGURE 2 | Morphology, thickness, and thermal/IR characterization of coatings and precursors. SEM images of the coatings annealed for different durations: (A) 30, (B) 60, (C) 90, and (D) 120 min, (E–H) along with the corresponding thickness distribution mappings. Infrared transmission spectra of the $VO(C_2O_4)\cdot 2H_2O$ precursor (I) before and (J) after Bi^{3+} incorporation. (K) TGA curves of $VO(C_2O_4)\cdot 2H_2O$, Bi-$VO(C_2O_4)\cdot 2H_2O$, and $Bi_2(SO_4)_3$; (L) corresponding DTA curves.

coating thickness remained overall uniform, first increasing from 84 to 138 nm and then slightly decreasing to 127 nm.

To further clarify the formation mechanism of the composite micro-nano structure, the physicochemical properties of the precursors were systematically analyzed. Figure 2I,J presents the infrared transmission spectra of the $VO(C_2O_4)\cdot 2H_2O$ precursor before and after Bi^{3+} incorporation. Upon Bi^{3+} addition, the absorption peaks of C=O and V–O bonds shifted, whereas those of C–O and V=O remained almost unchanged, indicating that Bi^{3+} coordinated primarily with C=O and V–O groups. Thermogravimetric analysis (TGA) revealed that the

decomposition temperature of pure $VO(C_2O_4)\cdot 2H_2O$ was 317.3°C, which increased to 358.5°C after $Bi_2(SO_4)_3$ addition (Figure 2K,L), further confirming the formation of a more stable coordination compound. During subsequent thermal treatment, $VO(C_2O_4)\cdot 2H_2O$ first decomposed into VO_2, followed by decomposition of the Bi-$VO(C_2O_4)$ coordination compound, which then grew on the preformed VO_2 nanoparticles, ultimately yielding VO_2@$BiVO_4$ core–shell structures. This in situ preparation method results in the composite coating exhibiting adhesion and mechanical robustness of the hierarchical composite film, so that no delamination or peeling occurs after cross-cutting and tape removal after the standard tape test (Supporting Information S1: Figure S4).

3.2 | Optical Performance

The optical properties of the composite coatings were characterized using a UV–Vis–NIR spectrophotometer. Figure 3A shows the transmittance spectra of samples with different Bi:V molar ratios at low and high temperatures, with the corresponding T_{lum} and ΔT_{sol} summarized in Table 1. Increasing the Bi:V ratio from 0% to 10% led to an increase in T_{lum} from 43.4% to 52.4% and ΔT_{sol} from 8.9% to 15.6%, primarily attributed to the lighter color of $BiVO_4$ and the improved dispersion of VO_2. Further increasing the Bi:V ratio to 20% resulted in a slight decrease in ΔT_{sol} due to the reduced VO_2 content, whereas T_{lum} increased to 62.8%. At a Bi:V ratio of 30%, both T_{lum} and ΔT_{sol} decreased significantly.

Figure 3B presents the transmittance spectra of the sample with a Bi:V ratio of 20% after different annealing durations. With increasing annealing time, both T_{lum} and ΔT_{sol} first increased and then slightly decreased, which can be ascribed to the formation and disappearance of the porous nanosheet layer on the

TABLE 1 | Optical properties of samples under different conditions (optimal performance at 60 min).

	T_{lum} (%)		T_{sol} (%)		
Sample	**25°C**	**90°C**	**25°C**	**90°C**	**ΔT_{sol} (%)**
0%	43.4	44.1	48.1	39.2	8.9
10%	52.4	47.4	59.3	43.7	15.6
20%	62.8	58.3	69.5	54.8	14.7
30%	55.7	55.4	62.6	51.9	10.7
30 min	58.6	56.2	63.5	52.8	10.7
60 min	**62.4**	**57.4**	**69.3**	**53.7**	**15.6**
90 min	62.8	58.3	69.5	54.8	14.7
120 min	60.6	57.3	66.5	55.3	11.2

Note: The bold values indicate the best performance data of each group of samples in this work.

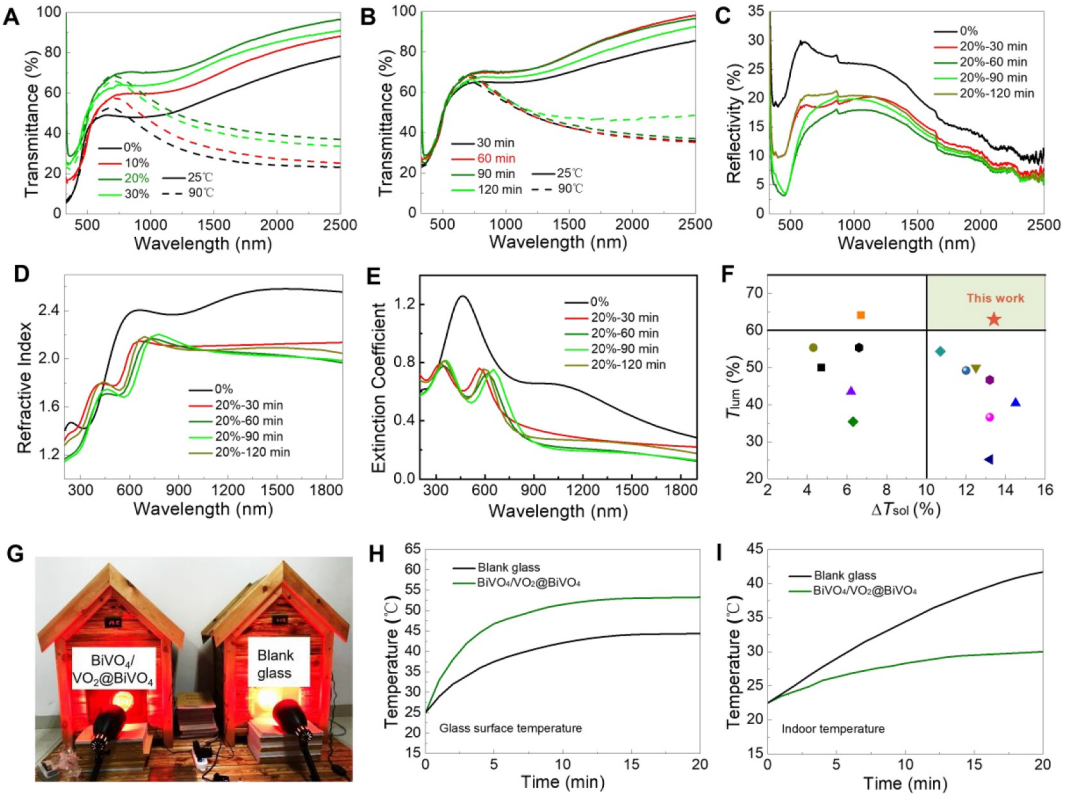

FIGURE 3 | Optical properties and thermal regulation performance of $BiVO_4/VO_2$@$BiVO_4$-coated samples. (A) Transmittance spectra of samples with different Bi:V molar ratios. (B) Transmittance spectra of samples with a Bi:V ratio of 20% under different annealing durations. (C) Reflectance, (D) refractive index, and (E) extinction coefficient of the corresponding samples. (F) Comparison of optical performance with literature reports. (G) Schematic of the miniature model house used to evaluate thermal regulation for bare glass and $BiVO_4/VO_2$@$BiVO_4$-coated glass. (H) Surface temperature of bare and $BiVO_4/VO_2$@$BiVO_4$-coated glass as a function of irradiation time. (I) Interior temperature of model houses with bare glass or $BiVO_4/VO_2$@$BiVO_4$-coated glass windows under irradiation.

surface, leading to an initial reduction followed by an increase in surface reflectance (Figure 3C). The extinction spectra of the samples annealed with different annealing times are calculated from the transmittance spectra of the R phase (Supporting Information S1: Figure S5). An obvious LSPR can be seen at 0.83 eV for the sample annealed for 120 min. For samples annealed for 30, 60, and 90 min, no obvious extinction peak is observed. However, the transmittance of the sample annealed for 120 min in the range of 1200–1500 nm is not lower than that of the samples annealed for 30, 60, and 90 min. This means that the samples annealed for 30, 60, and 90 min combine both the 1200–1500-nm low transmittance of resonant absorption and the 1500–2000-nm low transmittance of the continuous film. Compared with the pure VO_2 coating, the $BiVO_4/VO_2@BiVO_4$ composite exhibits a significantly lower refractive index and extinction coefficient (Figure 3D,E). The refractive index of the VO_2-based films does not change monotonically, which is consistent with the trend in the literature [38–40]. Optimal performance was achieved after 60 min of annealing, with T_{lum} and ΔT_{sol} reaching 62.4% and 15.6%, respectively, surpassing previously reported values (Figure 3F) [41–44]. To better demonstrate the advantages of the $BiVO_4/VO_2@BiVO_4$ composite coating, VO_2, $VO_2@BiVO_4$, and $BiVO_4/VO_2@BiVO_4$ are systematically compared. SEM images clearly reveal the structural evolution from a single $BiVO_4$ coating to a hierarchical nanoflake architecture formed by controlled annealing (Supporting Information S1: Figure S6a,b). Furthermore, comparative optical measurements demonstrate that the $BiVO_4/VO_2@BiVO_4$ film exhibits the highest visible-light transmittance (380–780 nm) and the strongest solar modulation ability, followed by $VO_2@BiVO_4$, whereas pristine VO_2 shows the poorest performance (Supporting Information S1: Figure S6c). These trends directly correlate with the hierarchical nanostructure.

To further evaluate the thermal regulation capability of the composite coating, a miniature model house was constructed (Figure 3G), with windows made of either the composite-coated glass or bare glass. Upon irradiation with a 180-W infrared lamp at a fixed distance of 40 cm, thermocouples recorded both the glass surface and interior temperatures. The composite-coated glass exhibited a faster surface temperature rise than the bare glass, whereas the interior temperature remained significantly lower. After 20 min of irradiation, the surface temperature of the composite-coated glass was 9.3°C higher than that of bare glass (Figure 3H), whereas the interior temperature was 11.7°C lower (Figure 3I), demonstrating the $BiVO_4/VO_2@BiVO_4$ composite coating's effectiveness in modulating indoor temperature.

To further elucidate the influence of the composite coating's hierarchical structure on its optical performance, finite-difference time-domain (FDTD) simulations were performed to model the transmittance and directly assess the effect of spatial architecture on light propagation. Figure 4A–C depicts the models of a dense VO_2 coating, a VO_2-$BiVO_4$ embedded composite coating, and the hierarchical $BiVO_4/VO_2@BiVO_4$ superstructure, respectively, where the VO_2 nanoparticles are 50 nm in diameter and the $BiVO_4$ nanosheet layers are 100 nm × 100 nm with gaps of 25 nm × 25 nm. Figure 4A1–C1, A2–C2 shows the corresponding electric-field distributions and transmittance spectra. The results indicate that under high-temperature conditions, the hierarchical composite coating exhibits significantly stronger light absorption than the dense VO_2 film, as clearly highlighted in the transmittance spectra (red arrows in Figure 4A2–C2). Moreover, compared with the embedded composite coating, the nanosheet layer on the superstructured surface substantially enhances visible-light transmittance. The simulation results are in excellent agreement with experimental observations, further confirming the crucial role of the micro-nano architecture in regulating the optical performance of the coatings. In addition, the relationships between nanosheet morphology (thickness, density, orientation) and visible transmittance are further simulated (Supporting Information S1: Figure S7).

3.3 | Self-Cleaning Performance

In addition, the optical absorption spectrum of the VO_2 film has an absorption edge around 500 nm. The corresponding Tauc plot derived from this spectrum (Supporting Information S1: Figure S9) indicates an optical band gap of 2.42 eV for the VO_2 film [45–47]. In comparison, the absorption edge of the composite film extends to approximately 580 nm, corresponding to an optical band gap of 2.12 eV (Supporting Information S1: Figure S10). This indicates that the composite film has a significantly broader light absorption range, which is favorable for photocatalytic reactions. The self-cleaning capability of the $BiVO_4/VO_2@BiVO_4$ composite coating was systematically evaluated using the photocatalytic degradation of methyl orange (MO) as a model pollutant. As shown in Figure 5A, MO exhibits a characteristic absorption peak at ~463 nm. Upon illumination for 0–3.0 h, the peak gradually diminishes and nearly disappears. The inset photograph shows the solution color changing from deep yellow to colorless, consistent with the spectral changes, indicating that the $BiVO_4/VO_2@BiVO_4$ composite coating possesses pronounced photocatalytic degradation activity toward MO. A comparison of the photocatalytic performance between the VO_2 single-layer film and the $BiVO_4/VO_2@BiVO_4$ composite film (Figure 5B) reveals that the latter exhibits significantly enhanced activity. This enhancement is attributed to the synergistic effect between VO_2 and $BiVO_4$ in terms of band structure alignment and charge carrier separation efficiency (Supporting Information S1: Figure S8), which promotes the effective separation and migration of photogenerated electron-hole pairs, enabling efficient MO degradation. Moreover, after at least six repeated photocatalytic cycles, the degradation efficiency of the $BiVO_4/VO_2@BiVO_4$ composite film shows negligible decline (Figure 5C), demonstrating excellent stability and recyclability and highlighting its practical application potential.

Similarly, as shown in Figure 5D–F, the $BiVO_4/VO_2@BiVO_4$ composite film exhibits outstanding photocatalytic degradation toward methylene blue (MB). With prolonged illumination, the characteristic absorption peak of MB at 664 nm gradually decreases, and the solution color fades from blue to colorless, confirming efficient MB molecule decomposition. Compared with the VO_2 single-layer film, the degradation rate of the composite film is markedly improved, further verifying that the synergistic interaction between VO_2 and $BiVO_4$ substantially enhances photocatalytic activity. Subsequently, the photocatalytic degradation kinetics was quantitatively analyzed based on the

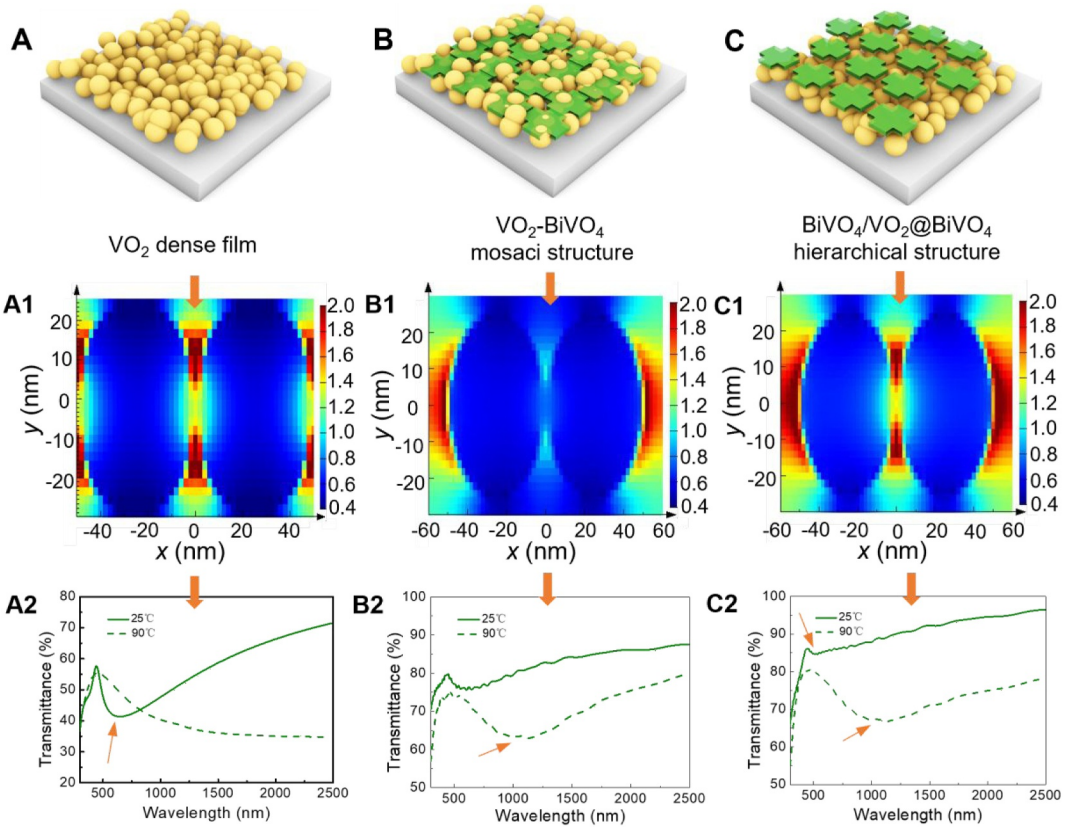

FIGURE 4 | Structural models, electric-field simulations, and transmittance of VO_2-based coatings. Models of (A) dense VO_2 coating, (B) VO_2-$BiVO_4$ embedded composite coating, and (C) $BiVO_4/VO_2@BiVO_4$ hierarchical superstructured coating. Simulated electric-field distributions under (A1–C1) high-temperature conditions and (A2–C2) corresponding transmittance spectra.

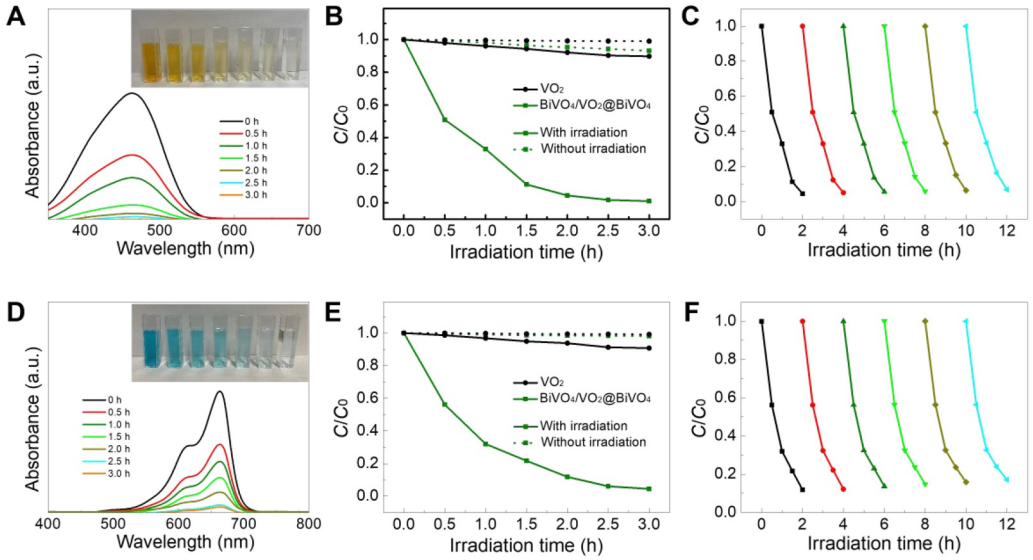

FIGURE 5 | Photocatalytic performance and stability of $BiVO_4/VO_2@BiVO_4$ composite films for MO and MB degradation. (A) Time-dependent UV–Vis absorption spectra of MO degradation over the $BiVO_4/VO_2@BiVO_4$ composite film; the inset shows photographs of the MO solution at corresponding illumination times. (B) Comparison of photocatalytic activity for MO degradation between VO_2 single-layer and $BiVO_4/VO_2@BiVO_4$ composite films. (C) Cycling stability of MO degradation over the $BiVO_4/VO_2@BiVO_4$ composite film. (D) Time-dependent UV–Vis absorption spectra of MB degradation over the $BiVO_4/VO_2@BiVO_4$ composite film; the inset shows photographs of the MB solution at corresponding illumination times. (E) Comparison of photocatalytic activity for MB degradation between VO_2 single-layer and $BiVO_4/VO_2@BiVO_4$ composite films. (F) Cycling stability of MB degradation over the $BiVO_4/VO_2@BiVO_4$ composite film.

degradation curves (Supporting Information S1: Figure S10). The apparent reaction rate constants (k) were calculated by fitting the experimental data using a pseudo-first-order kinetic model [48–50].

In addition to organic pollutant degradation, practical self-cleaning surfaces should also possess antimicrobial activity [51–53]. To further evaluate the comprehensive self-cleaning functionality, the photocatalytic antibacterial performance of the $BiVO_4/VO_2@BiVO_4$ composite coating was investigated. As shown in Figure 6A, bacterial suspensions were dropped onto bare glass, VO_2-coated glass, and $BiVO_4/VO_2@BiVO_4$ composite-coated glass, followed by visible-light illumination for 40 min. The coatings were then stamped onto nutrient agar plates and incubated at 37°C for 18 h to allow bacterial growth. Dense bacterial colonies were observed on bare glass, whereas VO_2-coated glass exhibited significantly reduced colony numbers, and the $BiVO_4/VO_2@BiVO_4$ composite coating showed almost no colony formation, demonstrating excellent photocatalytic bactericidal activity.

Figure 6B illustrates the mechanism of photocatalytic sterilization. Upon light irradiation, the composite coating absorbs photons to generate electron-hole pairs, which further react with water and oxygen molecules on the surface to produce highly reactive oxygen species (ROS). These ROS, owing to their strong oxidative capacity, can damage bacterial cell membranes and internal structures, leading to efficient bacterial inactivation. SEM observations (Figure 6C) reveal that *E. coli* cells on the composite coating surface exhibit significant shrinkage and structural damage under light irradiation, with compromised membrane integrity resulting in pronounced loss of cell viability.

The bacterial colony counts as a function of irradiation time are shown in Figure 6D, indicating a marked decrease with prolonged illumination. Analysis of the inactivation curves (Figure 6E) shows that the composite coating achieves 100% inactivation of *E. coli* within 40 min, whereas *S. aureus* is completely inactivated after 50 min, demonstrating high-efficiency bactericidal activity against both Gram-negative and Gram-positive bacteria. Moreover, the composite film maintains excellent stability under repeated use, retaining full antibacterial activity against both *E. coli* and *S. aureus* after six photocatalytic cycles (Supporting Information S1: Figure S12).

The $BiVO_4/VO_2@BiVO_4$ composite coating thus exhibits dual self-cleaning functionality, effectively degrading organic pollutants while simultaneously suppressing microbial attachment and growth. This multifunctionality provides a promising strategy for designing durable, self-maintaining smart surfaces, such as energy-efficient smart windows and environmental purification systems.

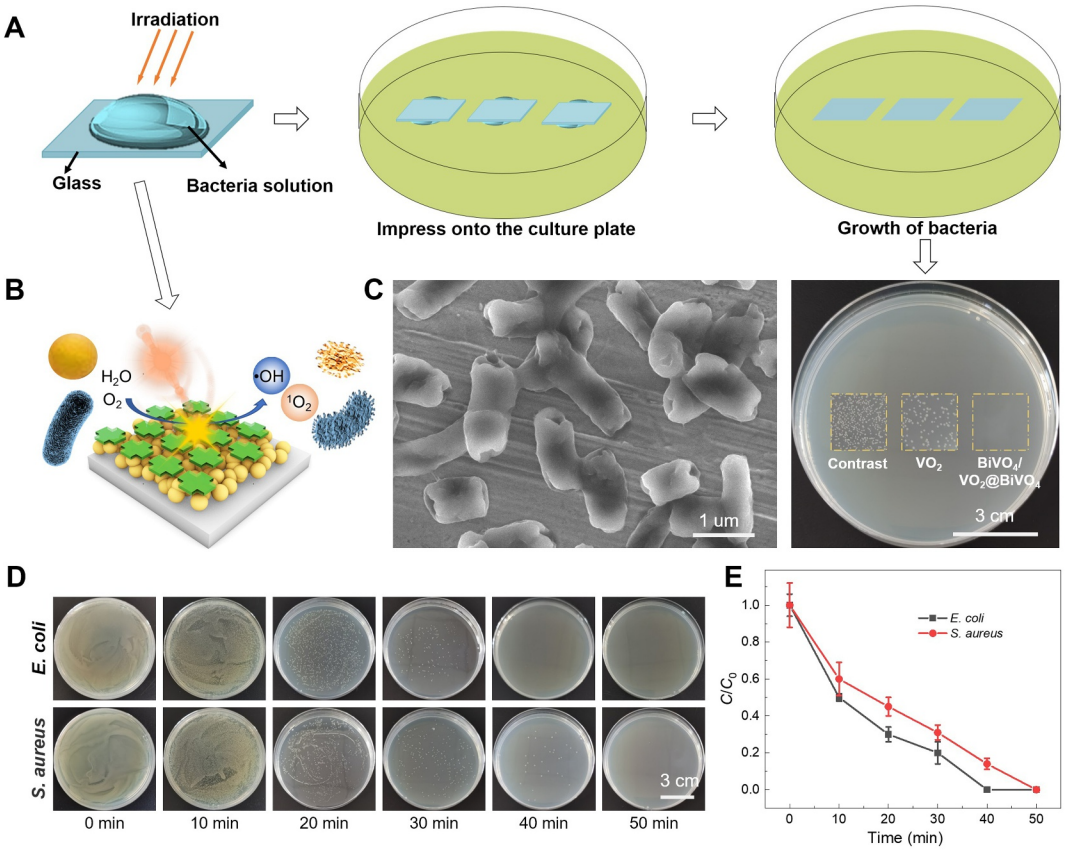

FIGURE 6 | Photocatalytic antibacterial activity and mechanism of the $BiVO_4/VO_2@BiVO_4$ composite coating. (A) Photocatalytic antibacterial activity of the $BiVO_4/VO_2@BiVO_4$ composite coating. (B) Schematic illustration of the photocatalytic bactericidal mechanism. (C) SEM images of *Escherichia coli* on the composite coating surface after light irradiation. (D) Photographs of bacterial colonies of *E. coli* and *Staphylococcus aureus* at different irradiation times. (E) Inactivation curves of *E. coli* and *S. aureus* under visible light irradiation.

3.4 | Environmental Durability

The environmental durability of the $BiVO_4/VO_2@BiVO_4$ composite coatings was systematically evaluated under accelerated aging conditions. Figure 7A,B shows the transmittance spectra of VO_2 and $BiVO_4/VO_2@BiVO_4$ coatings aged at 100°C and 50% relative humidity (RH) for different durations. After 4 days of aging, the ΔT_{sol} of the pure VO_2 coating decreased by ~80%, whereas the $BiVO_4/VO_2@BiVO_4$ composite coating retained ~80% of its initial ΔT_{sol} even after 27 days.

The long-term lifetime of the composite coating was further estimated using the Hallberg–Peck accelerated aging model [54, 55]:

$$AF = \exp\left[\frac{E_a}{k} * \left(\frac{1}{T_{use}} - \frac{1}{T_{test}}\right)\right] * \left(\frac{RH_{test}}{RH_{use}}\right)^n,$$

where AF is the acceleration factor; E_a is the activation energy (0.7 eV for VO_2); k is the Boltzmann constant (8.617×10^{-5} eV K^{-1}); n is the humidity acceleration exponent (taken as 3); and T_{use}, T_{test}, RH_{use}, and RH_{test} correspond to the working and test temperatures and humidities, respectively. Under the present conditions (T_{test} = 373 K, T_{use} = 298 K, RH_{test} = RH_{use} = 50%), the acceleration factor was calculated to be AF = 239.8, yielding an estimated service lifetime of $27 \times 239.8 \approx 6474$ days (~17 years). This demonstrates that the $BiVO_4/VO_2@BiVO_4$ coating can maintain ~80% of its solar modulation performance over nearly 2 decades, highlighting its excellent environmental stability, primarily attributed to the protective $VO_2@BiVO_4$ core–shell structure.

To further verify its practical application stability, the thermal hysteresis behavior of VO_2 during the phase transition, UV exposure, and freeze-thaw cycling was systematically investigated. Supporting Information S1: Figure S13 shows the resistivity of the $BiVO_4/VO_2@BiVO_4$ composite film as a function of temperature. The hysteresis width is 18.9°C. After 100 cycles of thermal cycling between 20°C and 100°C, the phase transition functionality of the composite film is preserved, and the phase transition temperature and the hysteresis width remain almost unchanged, which highlights its superior cycling stability.

A UV aging and freeze-thaw cycle aging test has also been conducted. The stability of the $BiVO_4/VO_2@BiVO_4$ composite film was examined in a UV aging box (QUV) under UV exposure. The test has been conducted continuously for 10 h, which is equivalent to a 12-day solar exposure. The results show that there is no significant change in the transmittance spectrum of the $BiVO_4/VO_2@BiVO_4$ composite film before and after the UV exposure (Supporting Information S1: Figure S14a). The $BiVO_4/VO_2@BiVO_4$ composite film was also placed in airtight containers and incubated at 25°C for 1 h and then frozen at −25°C for 1 h for freeze-thaw cycle aging. A maximum moisture content of 40% was maintained during the aging process, and samples were collected after 20 cycles. The results show that there is no significant change in the transmittance spectrum of the $BiVO_4/VO_2@BiVO_4$ composite film before and after freeze-thaw cycling aging (Supporting Information S1: Figure S15b). The results prove that the $BiVO_4/VO_2@BiVO_4$ composite film has a relatively stable optical property against UV radiation and freeze-thaw cycling.

In addition, the water contact angle of the $BiVO_4/VO_2@BiVO_4$ coating is significantly higher than that of pure VO_2 (Supporting Information S1: Figure S15), indicating improved hydrophobicity, which further contributes to enhanced durability. X-ray diffraction (XRD) patterns (Figure 7C) show that the diffraction peak positions and intensities of the composite coating remain nearly unchanged after aging, with no new impurity peaks observed, confirming excellent phase stability. The water contact angle after aging was 82.7° (Figure 7D), demonstrating that surface chemistry and wettability were largely preserved. SEM observations (Figure 7E,F) further revealed that the particle morphology and distribution of the

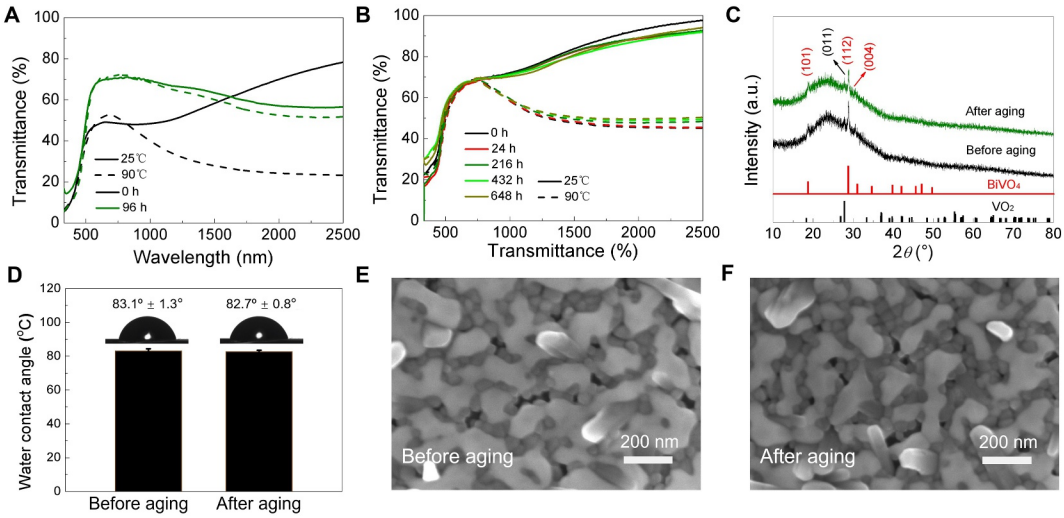

FIGURE 7 | Environmental stability and structural characterization of VO_2 and $BiVO_4/VO_2@BiVO_4$ coatings. Transmittance spectra of (A) the VO_2 coating and (B) the $BiVO_4/VO_2@BiVO_4$ composite coating after aging for different durations. (C) XRD patterns of the composite coating before and after aging. (D) Water contact angles of the composite coating before and after aging. SEM images of the composite coating (E) before aging and (F) after aging.

coating remained intact, without noticeable aggregation, cracking, or structural damage, indicating outstanding microstructural stability.

Collectively, these results confirm that the $BiVO_4/VO_2@BiVO_4$ composite coating exhibits superior stability compared with pure VO_2 coatings across multiple aspects, including optical performance, phase structure, surface wettability, and microstructural integrity.

4 | Conclusions

In summary, a hierarchical "core–shell-nanosheet" $BiVO_4/VO_2@BiVO_4$ composite coating was constructed via a coordination-compound-based controlled synthesis strategy. This structure ingeniously integrates the thermochromic properties of VO_2 with the antireflection-transmission enhancement and photocatalytic functionalities of $BiVO_4$, achieving multidimensional synergistic structure–property optimization. The resulting coating exhibits a high T_{lum} of 63.0% alongside a ΔT_{sol} of 15.6%, effectively overcoming the conventional trade-off between high transparency and strong modulation in VO_2-based smart windows. The $VO_2@BiVO_4$ core–shell layer significantly suppresses VO_2 oxidation and aggregation, allowing the coating to retain ~80% of its modulation performance after 27 days of aging at 100°C and 50% relative humidity, corresponding to an estimated service life of over 17 years. The outer porous $BiVO_4$ nanosheets further enhance transmittance via antireflection-transmission effects and impart excellent photocatalytic activity, achieving $>$ 90% degradation of organic dyes within 2 h of illumination and $>$ 99% inactivation of both *S. aureus* and *E. coli*. This work demonstrates the synergistic optimization of optical performance, environmental stability, and self-cleaning antibacterial capability, providing a feasible pathway for the practical application of VO_2-based smart windows and offering new insights into the micro/nanostructural design and functional integration of multifunctional composite films.

Author Contributions

Huiyan Xu: conceptualization, resources. **Lihan Cai:** writing – original draft. **Jian Zhang:** writing – original draft. **Rui Chen:** conceptualization. **Zaoyang Xu:** investigation. **Mingyu Lu:** data curation. **Xinyuan Xing:** conceptualization. **Shuaijun Yang:** data curation. **Tongyao Liu:** data curation. **Yuanwei Sun:** data curation. **Xuchuan Jiang:** writing – review and editing. **Xin Yu:** funding acquisition, writing – review and editing.

Acknowledgments

This study was financially supported by the National Natural Science Foundation of China (Grant Nos. 52422213 and 52272212), the Natural Science Foundation of Shandong Province (Grant Nos. ZR2022JQ20 and ZR2025QC589), and the Taishan Scholar Project of Shandong Province (Grant No. tsqn202211168).

Conflicts of Interest

The authors declare no conflicts of interest.

Data Availability Statement

The data that support the findings of this study are available from the corresponding author upon reasonable request.

References

1. S. Tan, S. Guo, Y. Wu, T. Zhang, J. Tang, and G. Ji, "Achieving Broadband Microwave Shielding, Thermal Management, and Smart Window in Energy-Efficient Buildings," *Advanced Functional Materials* 35, no. 8 (2025): 2415921, https://doi.org/10.1002/adfm.202415921.

2. Z. Zhang, L. Zhang, Y. Zhou, et al., "Thermochromic Energy Efficient Windows: Fundamentals, Recent Advances, and Perspectives," *Chemical Reviews* 123, no. 11 (2023): 7025–7080, https://doi.org/10.1021/acs.chemrev.2c00762.

3. K. Lei, Q. Jiang, D. Gong, et al., "Hydrogel Smart Windows: Working Mechanisms, Recent Developments, and Perspectives," *Small* 21, no. 48 (2025): e10382, https://doi.org/10.1002/smll.202510382.

4. C. Jiang, L. He, Q. Xuan, Y. Liao, J.-G. Dai, and D. Lei, "Phase-Change VO_2-Based Thermochromic Smart Windows," *Light: Science & Applications* 13, no. 1 (2024): 255, https://doi.org/10.1038/s41377-024-01560-9.

5. V. Devthade and S. Lee, "Synthesis of Vanadium Dioxide Thin Films and Nanostructures," *Journal of Applied Physics* 128, no. 23 (2020): 231101, https://doi.org/10.1063/5.0027690.

6. M. Li, S. Magdassi, Y. Gao, and Yi Long, "Hydrothermal Synthesis of VO_2 Polymorphs: Advantages, Challenges and Prospects for the Application of Energy Efficient Smart Windows," *Small* 13, no. 36 (2017): 1701147, https://doi.org/10.1002/smll.201701147.

7. J. Faucheu, E. Bourgeat-Lami, and V. Prevost, "A Review of Vanadium Dioxide as an Actor of Nanothermochromism: Challenges and Perspectives for Polymer Nanocomposites," *Advanced Engineering Materials* 21, no. 2 (2019): 1800438, https://doi.org/10.1002/adem.201800438.

8. X. Li, C. Cao, C. Liu, et al., "Self-Rolling of Vanadium Dioxide Nanomembranes for Enhanced Multi-Level Solar Modulation," *Nature Communications* 13, no. 1 (2022): 7819, https://doi.org/10.1038/s41467-022-35513-w.

9. J. Kim, K. Haeng Lee, D.-B. Seo, et al., "Two-Dimensional VO_2 Nanosheet Converted From MXene for Flexible Thermochromic Smart Windows," *Chemical Engineering Journal* 477 (2023): 147014, https://doi.org/10.1016/j.cej.2023.147014.

10. S. Liu, G. Chen, J. Li, and S.-J. Cao, "Smart Skin for Zero Energy Buildings: A Review of Thermoresponsive Spectral-Adaptive Envelopes," *Advanced Materials* 38, no. 3 (2026): e11392, https://doi.org/10.1002/adma.202511392.

11. X. Yu, C. Li, J. Zhang, L. Zhao, J. Pang, and L. Ding, "Recent Progress on Sn_3O_4 Nanomaterials for Photocatalytic Applications," *International Journal of Minerals, Metallurgy and Materials* 31, no. 2 (2024): 231–244, https://doi.org/10.1007/s12613-023-2761-z.

12. T. Chang, Y. Zhu, C. Cao, et al., "Multifunctional Flexible Vanadium Dioxide Films," *Accounts of Materials Research* 2, no. 9 (2021): 714–725, https://doi.org/10.1021/accountsmr.1c00044.

13. M. L. De Marco, O. Smith, F. Thorimbert, et al., "Self-Regulating VO_2 Photonic Pigments," *Chemistry of Materials* 35, no. 17 (2023): 7164–7174, https://doi.org/10.1021/acs.chemmater.3c01436.

14. Y. Ke, I. Balin, N. Wang, et al., "Two-Dimensional SiO_2/VO_2 Photonic Crystals With Statistically Visible and Dynamically Infrared Modulated for Smart Window Deployment," *ACS Applied Materials & Interfaces* 8, no. 48 (2016): 33112–33120, https://doi.org/10.1021/acsami.6b12175.

15. H. Xie and C. Fan, "Tunable and Adaptive Colored Radiative Cooler Based on the Phase Transition of VO_2 Photonic Design," *Solar Energy Materials and Solar Cells* 282 (2025): 113382, https://doi.org/10.1016/j.solmat.2024.113382.

16. Y. Su and J. He, "A Confined VO_2 Synthesis plus Liquid-Like Shielding Strategy for Durable, Omniphobic, and Multifunctional Smart Windows," *Chemical Engineering Journal* 519 (2025): 165146, https://doi.org/10.1016/j.cej.2025.165146.

17. Y. Ou, H. Ji, Y. Wang, et al., "Photothermal Synergistic Modulation of Patterned VO_2-Based Composite Films for Smart Windows," *Solar Energy* 279 (2024): 112808, https://doi.org/10.1016/j.solener.2024.112808.

18. Z. Khan, P. Singh, S. A. Ansari, S. R. Manippady, A. Jaiswal, and M. Saxena, "VO_2 Nanostructures for Batteries and Supercapacitors: A Review," *Small* 17, no. 4 (2021): 2006651, https://doi.org/10.1002/smll.202006651.

19. T. Chang, X. Cao, L. R. Dedon, et al., "Optical Design and Stability Study for Ultrahigh-Performance and Long-Lived Vanadium Dioxide-Based Thermochromic Coatings," *Nano Energy* 44 (2018): 256–264, https://doi.org/10.1016/j.nanoen.2017.11.061.

20. W. Jin, K. Park, J. Y. Cho, et al., "Thermochromic Properties of ZnO/VO_2/ZnO Films on Soda Lime Silicate Glass Deposited by RF Magnetron Sputtering," *Ceramics International* 49, no. 7 (2023): 10437–10444, https://doi.org/10.1016/j.ceramint.2022.11.226.

21. J. Keum, J. Choi, S. Kim, et al., "Innovative Dual-Band Energy-Efficient Smart Windows Using VO_2(M)-Based Fabry-Pérot Structures for Solar and Radiative Cooling Modulation," *Materials Today Physics* 52 (2025): 101665, https://doi.org/10.1016/j.mtphys.2025.101665.

22. B. Li, J. Liu, S. Tian, et al., "VO_2-ZnO Composite Films With Enhanced Thermochromic Properties for Smart Windows," *Ceramics International* 46, no. 3 (2020): 2758–2763, https://doi.org/10.1016/j.ceramint.2019.09.264.

23. J. Schläefer, C. Sol, T. Li, et al., "Thermochromic VO_2−SiO_2 Nanocomposite Smart Window Coatings With Narrow Phase Transition Hysteresis and Transition Gradient Width," *Solar Energy Materials and Solar Cells* 200 (2019): 109944, https://doi.org/10.1016/j.solmat.2019.109944.

24. R. Jiang, W. Cai, T. Zheng, et al., "Energy-Saving VO_2 Bilayer Films With Self-Cleaning and Self-Healing for Smart Windows," *ACS Applied Materials & Interfaces* 17, no. 19 (2025): 28743–28751, https://doi.org/10.1021/acsami.5c05493.

25. Y. Zhao, H. Ji, Y. Ou, et al., "Novel Sunlight-Driven Cu_7S_4/VO_2 Composite Films for Smart Windows," *Journal of Materials Chemistry C* 12, no. 7 (2024): 2534–2543, https://doi.org/10.1039/D3TC03774F.

26. Z. Qu, L. Yao, J. Li, et al., "Bifunctional Template-Induced VO_2@SiO_2 Dual-Shelled Hollow Nanosphere-Based Coatings for Smart Windows," *ACS Applied Materials & Interfaces* 11, no. 17 (2019): 15960–15968, https://doi.org/10.1021/acsami.8b22113.

27. Z. Qu, L. Yao, S. Ma, et al., "Rational Design of HSNs/VO_2 Bilayer Coatings With Optimized Optical Performances and Mechanical Robustness for Smart Windows," *Solar Energy Materials and Solar Cells* 200 (2019): 109920, https://doi.org/10.1016/j.solmat.2019.109920.

28. J. Zhang, T. Wang, W. Xu, et al., "Thermochromic VO_2–SiO_2 Composite Coating From Ammonium Citrato-Oxovanadate(IV)," *Nanotechnology* 32, no. 22 (2021): 225402, https://doi.org/10.1088/1361-6528/abe43a.

29. J. Kang, J. Liu, F. Shi, et al., "Facile Fabrication of VO_2/SiO_2 Aerogel Composite Films With Excellent Thermochromic Properties for Smart Windows," *Applied Surface Science* 573 (2022): 151507, https://doi.org/10.1016/j.apsusc.2021.151507.

30. B. Liu, X. Wang, Y. Zhang, et al., "A Standalone Bismuth Vanadate-Silicon Artificial Leaf Achieving 8.4% Efficiency for Hydrogen Production," *Nature Communications* 16, no. 1 (2025): 2792, https://doi.org/10.1038/s41467-025-58102-z.

31. B. Ramulu, A. R. Mule, S. J. Arbaz, and J. Su Yu, "Structural Design and Fabrication of Metal Vanadate Hydrates for Wearable Electronic Applications," *Chemical Engineering Journal* 467 (2023): 143498, https://doi.org/10.1016/j.cej.2023.143498.

32. Y. Xiao, S. Hu, Y. Liu, et al., "Pt-Modified $BiVO_4$ Nanosheets for Enhanced Acetone Sensing," *Sensors and Actuators B: Chemical* 389 (2023): 133853, https://doi.org/10.1016/j.snb.2023.133853.

33. M. Vijayalakshmi, R. Wang, K. Raghava Reddy, et al., "Aminabhavi, Hierarchical g-C_3N_4-Nanosheet-Covered Nickel Cobalt Vanadate Hydroxide Porous Fibrous Array Hybrid Electrodes for High Performance Asymmetric Supercapacitors," *Chemical Engineering Journal* 512 (2025): 162043, https://doi.org/10.1016/j.cej.2025.162043.

34. T. Zhang, M. Liu, Y. Ma, et al., "Nitrogen-Doped Carbon Quantum Dots Modified Cobalt Vanadate Nanosheets as Efficient Catalysts for Magnesium Hydride," *Chemical Engineering Journal* 522 (2025): 167952, https://doi.org/10.1016/j.cej.2025.167952.

35. Y. Liu, C. Xing, Z. Yao, et al., "Co-Doped Bismuth Vanadate/Zinc Tungstate Heterojunction With Dual Internal Electric Fields for Efficient Photocatalytic Reduction of Carbon Dioxide," *Journal of Colloid and Interface Science* 677 (2025): 1095–1106, https://doi.org/10.1016/j.jcis.2024.08.142.

36. J. Pan, Z. Zhang, Z. Yao, et al., "Potential Modulation Strategy on Bismuth Vanadate-Based Semiconductor to Enhance Antibiotic Degradation in Heterogeneous Electro-Fenton System," *Chemical Engineering Journal* 493 (2024): 152617, https://doi.org/10.1016/j.cej.2024.152617.

37. Y. Deng, J. Wang, J. Wang, W. Wang, H. Zhang, and S. Yin, "Restricted Template–Induced Growth of Vanadium Oxide Clusters on $BiVO_4$ (110) Crystal Planes for an Efficient Catalytic Conversion of CO_2 to Methanol," *Chemical Engineering Journal* 496 (2024): 153963, https://doi.org/10.1016/j.cej.2024.153963.

38. J. John, A. Slassi, J. Sun, et al., "Tunable Optical Anisotropy in Epitaxial Phase-Change VO_2 Thin Films," *Nanophotonics* 11, no. 17 (2022): 3913–3922, https://doi.org/10.1515/nanoph-2022-0153.

39. N. R. Mlyuka, G. A. Niklasson, and C. G. Granqvist, "Thermochromic VO_2-Based Multilayer Films With Enhanced Luminous Transmittance and Solar Modulation," *Physica Status Solidi* 206, no. 9 (2009): 2155–2160, https://doi.org/10.1002/pssa.200881798.

40. Y. Xie, P. Jiang, K. Sun, W. Lu, Q. Lai, and J. Tan, "Influence of Incorporated Particles on the Optical Performance of VO_2 Nanoparticle-Based Thermochromic Films," *Optics Communications* 574 (2025): 131182, https://doi.org/10.1016/j.optcom.2024.131182.

41. T. Ren and C. Li, "VO_2-Based Temperature-Adaptive Radiative Materials Towards Real-World Applications: A Review," *Applied Energy* 399 (2025): 126540, https://doi.org/10.1016/j.apenergy.2025.126540.

42. Z. Li, Z. Zhang, and X. Zhou, "Chemical Modulation of Metal–Insulator Transition Toward Multifunctional Applications in Vanadium Dioxide Nanostructures," *Small* 19, no. 44 (2023): 2305234, https://doi.org/10.1002/smll.202305234.

43. X. Cao, T. Chang, Z. Shao, F. Xu, H. Luo, and P. Jin, "Challenges and Opportunities Toward Real Application of VO_2-Based Smart Glazing," *Matter* 2, no. 4 (2020): 862–881, https://doi.org/10.1016/j.matt.2020.02.009.

44. M. Alsaadi, K. Lerttraikul, S. Chatraphorn, and S. Kittiwatanakul, "Strategies for Enhanced Optical Performance and Durability of VO_2-Based Thermochromic Windows," *Advanced Engineering Materials* 26, no. 14 (2024): 2302224, https://doi.org/10.1002/adem.202302224.

45. F. Huang, W. Wang, G. Li, et al., "Exceptional Degradation of Organic Pollutant Through Piezoelectric Photocatalysis and Peroxymonosulfate Activation in the Designed $Bi_4O_5Br_2$/BCZT S-Scheme

Heterojunction," *Rare Metals* 44, no. 6 (2025): 3981–3994, https://doi.org/10.1007/s12598-024-03203-9.

46. S. Ishwaya, H. Nagaswarupa, Y. Naik, et al., "Multifunctional Applications of Barium Zinc Vanadate Nanoparticles for Photocatalytic Dye Degradation, Energy Storage and Sensing Applications," *International Journal of Minerals, Metallurgy and Materials* 32 (2025): 3052–3071, https://doi.org/10.1007/s12613-025-3160-4.

47. L. Ding, L. Wang, J. Zhang, et al., "Nanozymes Regulated by Nitrogen Element: Mechanism, Design, and Application," *Advanced Powder Materials* 3, no. 4 (2024): 100191, https://doi.org/10.1016/j.apmate.2024.100191.

48. Z. Yang, X. Zhang, L. Wang, et al., "Defect-Engineered CoFe Layered Double Hydroxide Quantum Dots: Oxygen Vacancy-Driven Boost in Peroxidase-Mimic Catalysis for Multiplex Biomarker Sensing," *ACS Materials Letters* 7, no. 5 (2025): 1777–1785, https://doi.org/10.1021/acsmaterialslett.4c02651.

49. Y. Li, X. Yu, Y. Zhou, Y. Lin, and Y. Wu, "Home International Journal of Minerals, Metallurgy and Materials Article Nanostructured ZnO/$BiVO_4$ I-Scheme Heterojunctions for Piezocatalytic Degradation of Organic Dyes via Harvesting Ultrasonic Vibration Energy," *International Journal of Minerals, Metallurgy and Materials* 32, no. 2 (2025): 488–497, https://doi.org/10.1007/s12613-024-2920-x.

50. Y. Gao, H. Zhao, M. Liu, et al., "Incorporating Co_3O_4/C Modified MnO_x/SiO_2 Into Tailored Sponge for Bifunctional Photothermal Water Evaporation and Pollutant Degradation," *Rare Metals* 44, no. 2 (2025): 1122–1138, https://doi.org/10.1007/s12598-024-02996-z.

51. H. Abdelhamid, "Metal-Organic Frameworks (MOFs) for Bone Treatment and Mineralization," *European Cells and Materials* 54 (2025): 91–114, https://doi.org/10.22203/eCM.v054a07.

52. L. Han, Z. Yuan, H. Ren, et al., "Infection-Responsive Polysaccharide-Based Drug-Loaded Nano-Assembly for Dual-Modal Treatment Against Drug-Resistant Bacterial Lung Infection," *BMEMat* 2, no. 3 (2024): e12120, https://doi.org/10.1002/bmm2.12120.

53. Z. Yang, L. Wang, X. Zhang, et al., "Nitrogen Vacancy Modulation of Tungsten Nitride Peroxidase-Mimetic Activity for Bacterial Infection Therapy," *ACS Nano* 18, no. 35 (2024): 24469–24483, https://doi.org/10.1021/acsnano.4c07856.

54. X. Zhou, Y. Meng, T. D. Vu, et al., "A New Strategy of Nanocompositing Vanadium Dioxide With Excellent Durability," *Journal of Materials Chemistry A* 9, no. 28 (2021): 15618–15628, https://doi.org/10.1039/D1TA02525B.

55. T. D. Vu, H. Xie, S. Wang, J. Hu, X. Zeng, and Yi Long, "Durable Vanadium Dioxide With 33-Year Service Life for Smart Windows Applications," *Materials Today Energy* 26 (2022): 100978, https://doi.org/10.1016/j.mtener.2022.100978.

Supporting Information

Additional supporting information can be found online in the Supporting Information section.

Supporting Information S1: rar270332-sup-0001-suppl-data.docx.